Ceria Nanocrystals Exposing Wide (100) Facets: Structure and Polarity Compensation

Yi Pan, Niklas Nilius, Christian Stiehler, Hans-Joachim Freund, Jacek Goniakowski, Claudine Noguera

Ceria Nanocrystals Exposing Wide (100) Facets: Structure and Polarity Compensation

Yi Pan, Niklas Nilius, Christian Stiehler, Hans-Joachim Freund*

Jacek Goniakowski, Claudine Noguera*

Dr. Y. Pan, Prof. N. Nilius, C. Stiehler, Prof. H.-J. Freund

Fritz-Haber-Institut der Max-Planck-Gesellschaft, Faradayweg 4-6, D-14195 Berlin, Germany

Prof. N. Nilius

Carl von Ossietzky Universität Oldenburg, Institut für Physik, D-26111 Oldenburg, Germany

Email: niklas.nilius@uni-oldenburg.de

Dr. J. Goniakowski, Prof. C. Noguera

CNRS, UMR 7588, Institut des Nanosciences de Paris, F-75005 Paris, France

Sorbonne Universités, UPMC Univ. Paris 06, UMR 7588, INSP, F-75005 Paris, France

Email: jacek.goniakowski@insp.jussieu.fr

KEYWORDS: Ceria nanocrystals, (100) termination, polarity, reduction, scanning tunneling microscopy, density functional theory

ABSTRACT:

Compact CeO_2(111) films grown on Ru(0001) can be transformed into well-shaped nanoparticles by annealing them in an oxygen-poor environment. With increasing temperature, the particles undergo a distinct shape evolution that finally leads to crystallites exposing wide (100) facets. The atomic structure of the (100) termination is determined with a combination of high-resolution scanning tunneling microscopy and density functional theory. Two surface reconstructions are identified that are compatible with the need to compensate for the intrinsic dipole of the (100) plane and with a substantial reduction of the oxide material. Our study provides insights into the rarely explored (100) surface of ceria, which can be considered as model system for studying chemical processes on the polar termination of reducible oxides.

1. INTRODUCTION

Cerium dioxide is a prototype material of a reducible oxide and stands as such in the focus of intense experimental and theoretical research.[1] Its facile reducibility gives rise to unique catalytic properties, being exploited in technologically relevant processes, such as the water-gas-shift reaction, the oxidation of hydrocarbons and the methanol conversion.[1] The microscopic origin of reducibility has been identified in the comparable stability of Ce^{3+} and Ce^{4+} ions in the oxide lattice, a fact that facilitates formation of oxygen vacancies.[2] The ceria surface therefore allows for effective oxygen exchange with the gas phase, explaining its high oxygen storage capacity and its suitability as catalyst in Mars-van-Krevelen type of reactions.

The oxygen storage capacity of ceria is tightly connected with the energetics of O vacancy formation, which in turn depends on the local binding environment of the O^{2-} ions.[3] From a thermodynamic point of view, defect formation is most costly on the closed-packed (111) surface that, not surprisingly, features the lowest free-energy of all ceria planes.[4-6] Oxygen removal becomes easier on the open and less stable (100) and (110) planes, where the O^{2-} ions have reduced coordination numbers. Also, the CeO_2/Ce_2O_3 phase transition proceeds more easily on these surfaces. The chemical activity of the different ceria planes essentially mirrors the energy barrier for oxygen removal. For example, Mullins *et al.* observed a much higher propensity for hydroxylation on the open (110) compared to the close-packed (111) surface.[7, 8] A similar conclusion was drawn from density functional theory (DFT) calculations, addressing the CO oxidation over various low-index ceria planes. Also these studies successfully correlated the Gibbs free energy of a given termination with the respective reaction yield.[9]

The most active, hence least stable ceria planes are typically not the ones that can be prepared and explored in experiment. In fact, most fundamental studies have been performed on CeO_2(111) that is easily prepared on Cu, Pt and Ru supports.[10-12] In contrast, the (110) and (100) surfaces were mainly explored on powder samples, implying that the desired low-stability planes

always occurred in combination with stable (111) regions.[13-15] Experiments on ceria (100) are further hampered by the intrinsic polarity of this termination,[16] and cancellation of the polar dipole often produces undefined surface configurations. So far, atomic-scale measurements on CeO_2(100) has been reported in a single scanning tunneling microscopy (STM) study,[17] while mainly transmission electron microscopy was used to characterize the (110) facets of ceria nanoparticles.[18, 19]

In this work, we discuss the structural and morphological properties of ceria crystallites that develop from flat CeO_2(111) films grown on Ru(0001) in a high-temperature dewetting process. The particles expose wide (100) planes, suitable for atomic-scale imaging with the STM. Appropriate structure models, accounting for the polar nature and possible non-stoichiometric compositions of the (100) termination, are derived from DFT calculations. Our work unravels unique properties of the rarely explored (100) surface of ceria.

2. RESULTS and DISCUSSION

2.1. Temperature dependent structure and morphology of ceria nanoparticles

The evolution of the ceria-covered Ru(0001) surface upon annealing is displayed in Figure 1. Starting from 800 K, hexagonal holes open up in the initially flat and homogenous CeO_2(111) film (Fig. 1a). At 900 K, the film dewets and exposes large areas of the pristine Ru support.[21] The remaining oxide islands are typically 100 nm in diameter and 1.5-1.8 nm in height. Their triangular or hexagonal shape indicates that the underlying lattice is still three-fold symmetric, hence of CeO_2(111) type. This assumption is supported by atomically resolved images, displaying the hexagonal arrangement of the surface Ce^{4+} ions (Fig. 1a, inset). At temperatures above 900 K, a new island type appears on the surface. It is distinguishable from the (111) patches by a larger height-to-diameter ratio and the presence of right-angled base planes (Fig. 1b). Apparently, the hexagonal (111) lattice is not the underlying structural element anymore. One of the two or-

thogonal axes of the new islands always aligns with the hexagonal Ru(0001) lattice, and three island orientations rotated by 120° can thus be found in the STM.

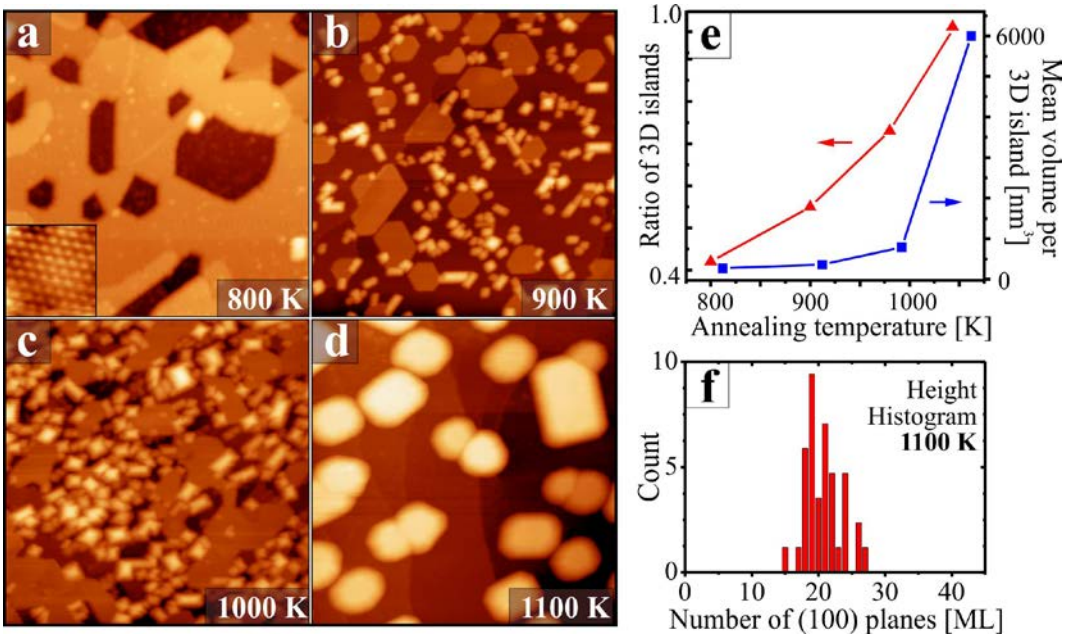

Figure 1. (a-d) Temperature series showing the evolution from a flat CeO_2(111) film to nanoparticles covered with (100) facets (5.0 V, 20 pA, 150 × 150 nm^2). The maximum annealing temperature is depicted in the panels. The inset in (a) displays the atomically resolved CeO_2(111) surface. (e) Ratio between flat CeO_2(111) islands and compact 3D crystallites as well as mean volume of the 3D deposits as a function of temperature. (f) Height histogram of the crystallites prepared by 1100 K annealing.

The new deposits are of pyramidal or prismatic shape and have square or rectangular base planes, respectively (Fig.2a). Their lateral size is restricted to 5-10 nm for annealing temperatures below 900 K, but increases to 25 nm upon 1000 K annealing. This enlargement is accompanied by changes in the particle shape that resembles more and more a truncated pyramid with flat top facet. Above 1000 K, the hexagonal islands completely disappear and the right-angled deposits become the dominant surface species. Their aspect ratio starts decreasing from 0.5 at 900 K to 0.25 at 1100 K, reflecting the development of flat top facets with up to 20 nm side length. In addition, the right-angled base planes of the deposits become octagonal and new side facets develop along the truncated edges (Fig. 2a).

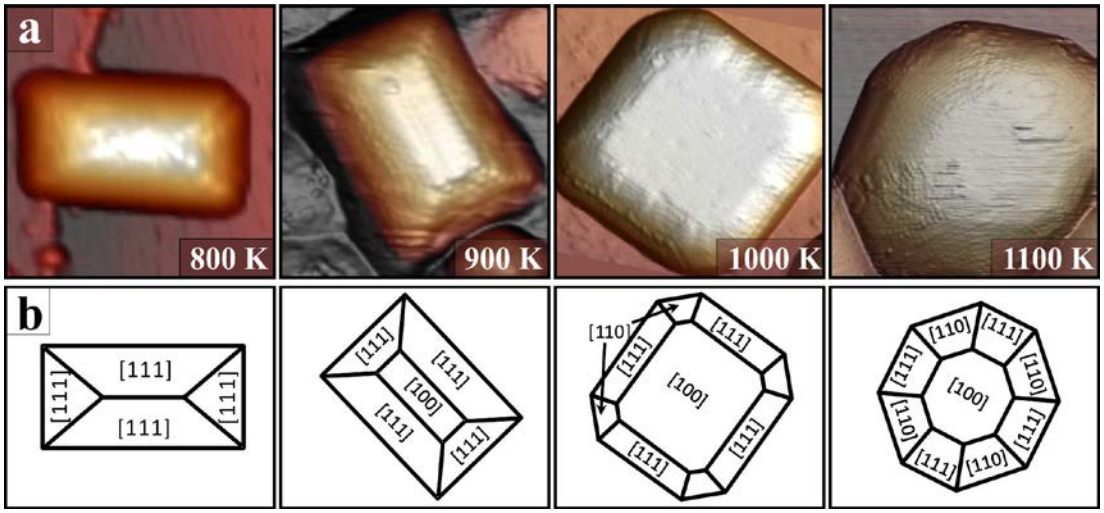

Figure 2. (a) 3D STM representations of ceria crystallites, as they appear at the given temperatures (5.0 V, 20 pA, left panels: 20 × 20 nm^2, right panels: 60 × 60 nm^2). (b) Corresponding structure models indicating the likely termination of exposed facets.

The end-point of this development is reached at 1100 K, when only 3D deposits with either octagonal or rectangular shape are found on the surface (Fig. 1d). Their lateral diameter has increased to 20-40 nm; their height converged to a surprisingly narrow range of 7±2 nm, equal to ~20 atomic planes (Fig. 1f). The particle top-facets are now large enough to image them with atomic resolution in STM, as shown below. Sample annealing beyond 1100 K causes the particles to shrink again, as ceria evaporation becomes a dominant process. Figure 1e summarizes the temperature evolution of the number density and volume of 3D ceria deposits with respect to flat (111) islands. Apparently, the transition to the square oxide patches starts at 800 K, but becomes significant only at temperatures above 1000 K.[22]

After discussing the growth morphology, we focus on the atomic configuration of the ceria crystallites. STM images of their top facets unambiguously reveal a square lattice that corresponds to a (100) termination and mirrors the right-angled particle shapes (Fig. 3). The square atom arrangement deviates from the hexagonal symmetry of Ru(0001) and CeO_2(111), indicating a negligible template effect of the substrate. Two different terminations are identified in our study. The dominant one exhibits a square pattern with 7.4 Å periodicity, corresponding to a (2×2) superstructure with respect to the primitive (1×1) cell of CeO_2 (Fig. 3a, b). Its vertical cor-

rugation amounts to 1.4 Å when measured across a surface defect. This value is larger than the height modulation within a single (100) plane, suggesting that more than one atomic layer is exposed. The second termination is less abundant and appears mainly on top of small crystallites or along domain boundaries and step edges inside the (2×2) phase (Fig. 3a, c). Also here, a square lattice is revealed, however with reduced periodicity (5.4 Å) and vertical corrugation (0.3 Å). The pattern is titled by 45° against the (2×2) phase and can thus be assigned to a c(2×2) superstructure with respect to the ideal (100) lattice. In addition to the two reconstructions, various surface defects have been identified in our data, as shown in Fig. 3d. The most prominent defect in the (2×2) phase is one missing building block, leaving behind a surface depression. Occasionally, the isolated minima merge to a defect line, which exhibits a new fine structure along its axis. As discussed below, these 1D defects mark a local transition from the (2×2) to the c(2×2) termination.

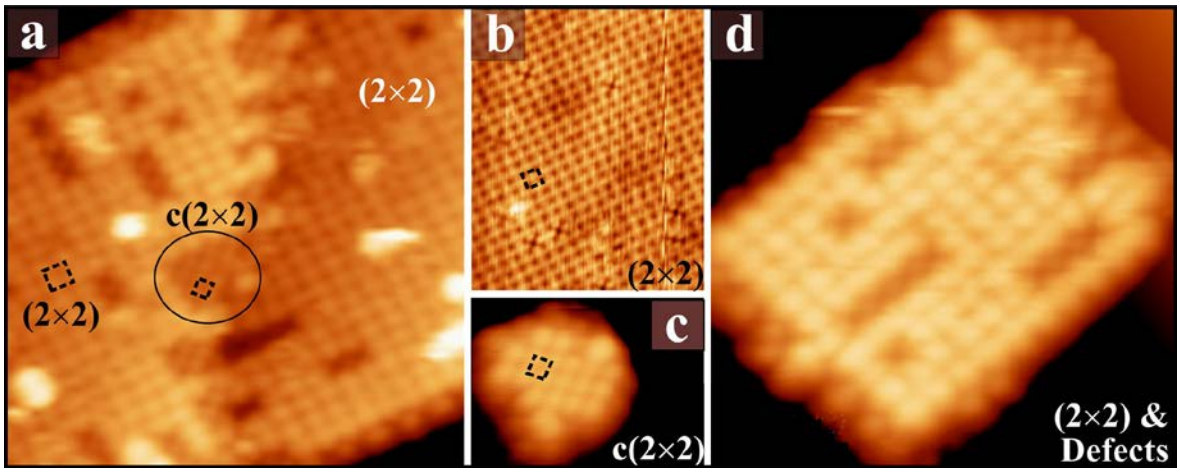

Figure 3. (a) Atomically resolved image of a large ceria crystallite exposing the (2×2) and c(2×2) surface pattern (5.0 V, 20 × 20 nm^2). (b, c) Close-up images of the (2×2) to a c(2×2) reconstruction with indicated unit cells. The image in (b) has been taken with an unusual tip and displays a slightly different contrast in which local defects have a cross-like appearance. (d) Atomically resolved (100) plane with typical surface defects (5.0 V, 12 × 12 nm^2).

Atomically resolved facets of the ceria crystallites always display one or the other surface reconstruction. This trend reflects the polar nature of the (100) plane in both, stoichiometric (CeO_2) and reduced ceria (bixbyite Ce_2O_3). In the two configurations, the (100) plane comprises alternat-

ing layers of cations and anions and develops a finite dipole moment. Structural changes that remove this surface dipole and stabilize the polar termination are discussed in the next paragraph.

2.2. Modeling of the (100) termination of ceria

Any surface model that aims at rationalizing the experimental results needs to account for the polarity of the (100) termination. The oppositely charged atom planes in the calcium fluorite lattice are equally spaced along the [100] direction and the polarity therefore cancels if the surface contains exactly half of the bulk charges.[16] As a starting point, we consider only Ce^{4+} and O^{2-} ions to be present in the surface and neglect possible reduction phenomena. With this constraint, the following complete set of structure models for the polar-compensated (2×2) CeO_2(100) plane can be developed (Fig. 4):

A0: (bulk CeO_2) - 4Ce - 8O - 2Ce (single-layer Ce-terminated)
B0: (bulk CeO_2) - 4Ce - 8O - 4Ce - 4O (single-layer O-terminated)
C0: (bulk CeO_2) - 4Ce - 6O - 1Ce (two-layer Ce-terminated)
D0: (bulk CeO_2) - 4Ce - 8O - 3Ce – 2O (two-layer O-terminated)

The single-layer models A0 and B0 have already been developed in the past, using either atomistic [4, 23, 24] or ab-initio calculations.[5, 6, 25] In both cases, the O termination was found to be thermodynamically preferred over the Ce termination and therefore used to explain the experimental results on CeO_2(100).[26, 27] Only for the (100) facets on ceria nanoparticles, as resolved in TEM,[19] a combination of O and Ce terminations was proposed. Beyond these early calculations, by performing a systematic structural optimization including position changes of all surface and sub-surface ions, we have revealed the following stability order for the stoichiometric (2×2) (100) structures as shown in Fig. 4: $\gamma_{C0} = 0.102$ eV/Å^2 < $\gamma_{B0} = 0.105$ eV/Å^2 < $\gamma_{A0} = 0.111$ eV/Å^2 < $\gamma_{D0} = 0.120$ eV/Å^2. The two-layer Ce-terminated surface (C0) turns out to be the most stable, although the energy difference between γ_{C0} and γ_{B0} is relatively small. On the other hand, the A0 and D0 structures are unlikely candidates for the experimental patterns given their higher Gibbs energy.

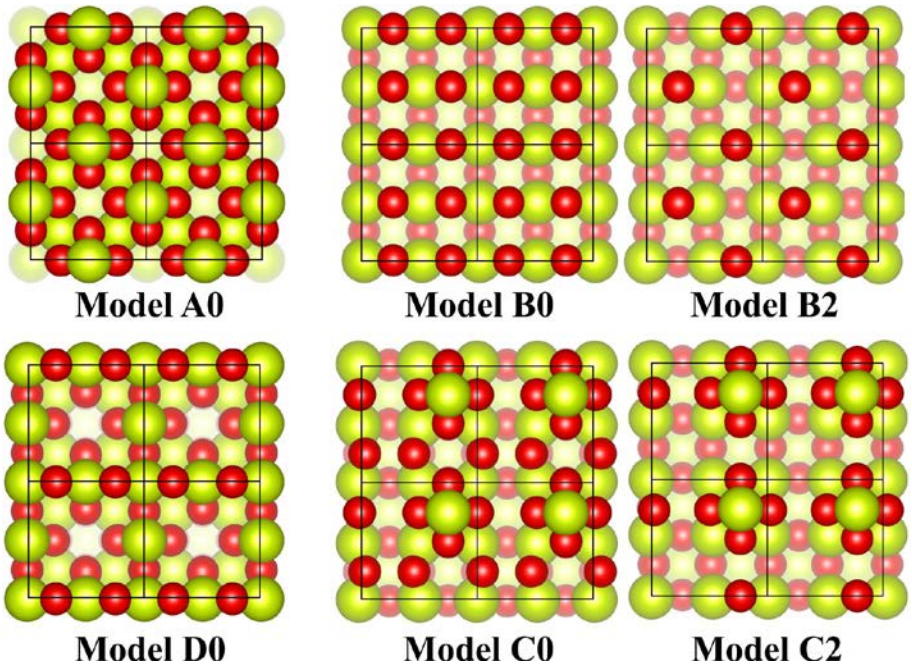

Figure 4. Polarity compensated, stoichiometric (A0-D0) and sub-stoichiometric (B2, C2) surfaces of CeO_2 (100). The small red and large yellow spheres denote the O and Ce ions, respectively. Each model covers a (2×2) unit cell.

In a second step, oxygen-lean configurations, representing the reduced oxide, have been obtained by removing O atoms from the stoichiometric surfaces. The resulting terminations contain both, Ce^{4+} and Ce^{3+} ions, in order to preserve charge-neutrality. Based on the four stoichiometric cases A0-D0, we have developed structure models An-Dn (n = 1-3), containing one, two or three O vacancies per (2×2) cell. We have systematically tested possible locations for the O defects in order to identify energetically preferred configurations. The calculations show that the stability order of the stoichiometric surfaces is, to a large extent, maintained in the oxygen-deficient structures (Fig. 5). This concerns, in particular, the two most stable structure families, C0-C3 and B0-B3, which are energetically favored over the entire range of O_2 chemical potentials. Moreover, type-C structures are systematically more stable than type-B ones. In the following section, we will discuss the two surfaces in detail and compare the computational and experimental results.

All type-C terminations are characterized by a single protrusion per (2×2) surface cell (Fig. 4). In the stoichiometric C0 surface, the maximum comprises a single nano-pyramid with a top-most Ce ion and four anions in the layer below. Such an atom arrangement is known as Wolf reconstruction,[28] and represents the common polarity compensation scheme for rocksalt (111) surfac-

es, *e.g.* MgO(111) and NiO(111).[29] In the oxygen-poor C1 and C2 structures, the pyramidal protrusion is preserved, while additional O defects occur in the surface layer. At higher degrees of reduction, surface and sub-surface vacancies become close in energy, resulting either in pyramids with three O^{2-} ions in the second layer or in four-atom based pyramids plus a subsurface defect.

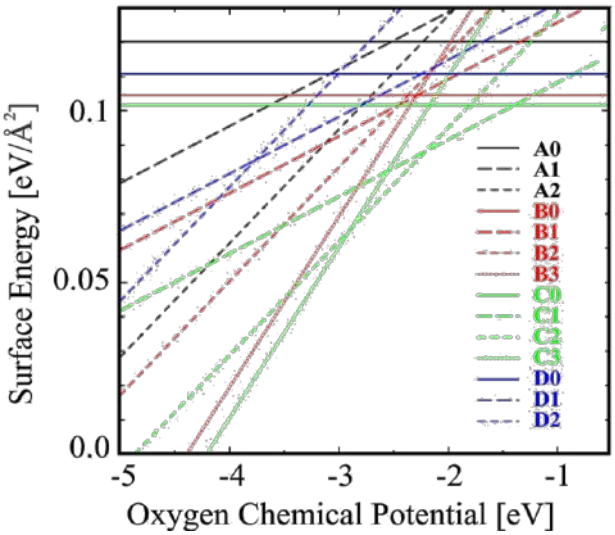

Figure 5. Gibbs free energy of all considered surface configurations as a function of the oxygen chemical potential.

The type-C configurations perfectly reproduce the experimental (2×2) pattern found on large (100) facets (Fig. 3a). However, even atomically resolved STM images are unable to distinguish between C0 to C3 structures, although the oxygen-poor C2 termination (Fig. 4) shows the best match due to its ideal four-fold symmetry. The latter contains a single maximum per (2×2) cell, now assigned to a CeO_4 pyramid, and features a height corrugation that is compatible with a two-layer structure. Moreover, the dominance of the (2×2) reconstruction in the experiment is in line with the systematic energetic preference of type-C structures in the calculations.

The c(2×2) reconstruction observed in STM can be linked to the second most stable, type-B configurations. The stoichiometric B0 structure contains 50% of the bulk O^{2-} ions in a chessboard-like arrangement and preserves the primitive (1×1) cell of CeO_2(100) (Fig. 4). Although considered to be the most stable polar-compensated (100) plane in the past,[4,6,27] its symmetry is in conflict with our findings. To reconcile symmetry properties with the experimental c(2×2) cell, O vacancies need to be introduced into the surface. Among the considered models, only the B2 structure in Fig. 4 shows perfect c(2×2) periodicity. Its single-layer nature matches the low height

corrugation (0.3 Å) found in the experiment. Also, the calculated energetic ordering, $\gamma_{C0} < \gamma_{B0}$, is in line with the experimental preference of the (2×2) with respect to the c(2×2) phase, the latter being exclusively found on small islands and along boundaries in the main termination. Note that the B3 structure with three O vacancies per (2×2) cell features a c(2×2) lattice only in the top plane, while a subsurface O defect breaks symmetry in the subsequent layers.

The C- and B-type configurations discussed above also account for defects in the (100) planes of the ceria crystallites (Fig. 3d). Both, line and point defects may be explained with confined swaps between the nano-pyramidal (C-type) and the isolated-anion (B-type) termination. Such transitions are realized by adding (removing) neutral CeO_2 units to (from) a given surface. For example, the C2 structure [layer sequence: bulk - 4Ce - 4O - 1Ce] transforms into a B2 termination [bulk - 4Ce - 2O] by removing one CeO_2 building block per (2×2) cell. Similarly, a nano-pyramid of the C2 structure is produced by adding a CeO_2 unit to a B2 surface and shifting an O^{2-} ion by one lattice position (Fig. 6).

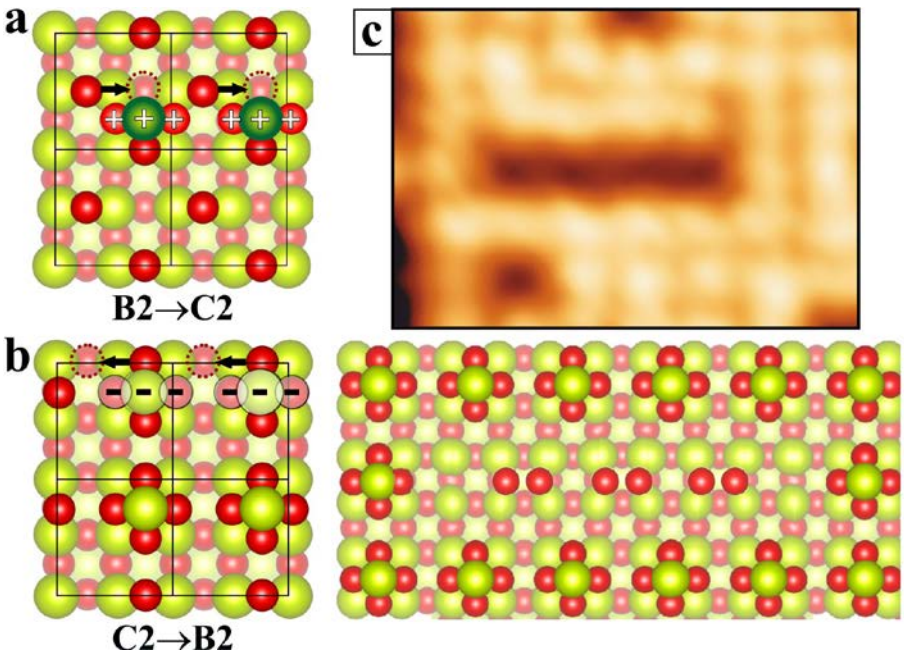

Figure 6. (a) Scheme for a local B2→C2 transition induced by adding the CeO_2 units marked with (+) to the surface and moving O^{2-} ions to adjacent lattice positions (see arrows). (b) Local C2→B2 transition, realized by desorbing the CeO_2 units marked by (-). (c) STM topography (3×2 nm^2) and corresponding ball model of a line defect in the (2×2) reconstruction.

Defects in the (2×2) reconstruction are tentatively assigned to such confined termination swaps (Fig. 6c). An isolated depression hereby reflects a missing CeO_2 unit, a change that neither alters the stoichiometry nor the dipole cancellation scheme. If adjacent CeO_2 blocks desorb, a trough appears in the surface that exposes a series of faint protrusions in out-of-phase positions with respect to the former nano-pyramids. The new maxima may represent bridge-bonded O^{2-} ions that have been shifted from their initial positions in the C2 structure. Continued desorption of CeO_2 units leads to the development of O-terminated (100) patches, a process that is however hindered by the unfavorable energetics of this termination. The c(2×2) domains therefore remain local perturbations in the main (2×2) phase, as corroborated by the experimental results.

The computational models of oxygen-deficient ceria surfaces reproduce the main properties of experimental (100) patches. In particular, the C2 and B2 structures explain well the periodicity, symmetry, and corrugation of the (2×2) and c(2×2) reconstruction found in STM, respectively. Despite this good correspondence, the reduction state of the ceria crystallites remains an open question in our study. Several indications point to a substantial reduction of the oxide during the annealing procedure. A first argument comes from the temperature-driven shape evolution that proceeds from exclusively (111)-terminated particles at 800 K to deposits with large (100) and (110) facets at higher temperature (Fig. 2b). Such geometry crossover is not compatible with the equilibrium shape of stoichiometric CeO_2, as predicted by the Gibbs-Wulff theorem.[30] In fact, the high surface energy of stoichiometric (100) compared to (111) planes (0.10 versus 0.05 eV/Å2) does not support the presence of (100) facets from a thermodynamic point of view. The formation of (100) and (110) planes rather indicates a progressive oxide reduction upon annealing. Secondly, the reduced configurations anticipated here (A3-D3) all contain O vacancies in the subsurface region. Their stability gain with respect to surface defects is a common trend and marks the transition from the CeO_2 to the Ce_2O_3 lattice.[31] In fact, a (100)-oriented oxygen layer in bixbyite Ce_2O_3 contains 6 anions per unit cell and can thus be considered as a (2×2) CeO_2(100)

plane with two missing O^{2-} ions. Given this similarity, the (100) termination of calcium-fluorite (CeO_2) and bixbyite lattices (Ce_2O_3) may not be distinguishable in STM.

As the reduction state of the ceria crystallites cannot be deduced from the experiment at this point, we will address the hypothesis of a full reduction by theoretical means. Starting from the bulk structure of bixbyite (100), composed of equidistant layers with either $4Ce^{3+}$ or $6O^{2-}$ ions per unit cell, only two polar-compensated terminations can be constructed:

I. (bulk Ce_2O_3) - 4Ce - 6O - 2Ce (single layer Ce-terminated)

II. (bulk Ce_2O_3) - 4Ce - 3O (single layer O-terminated)

The single-layer oxygen termination is model (II) is similar to the type-B configurations discussed before. However, an additional O vacancy would be necessary to produce the c(2×2) periodicity found in experiment, requiring a further reduction of the Ce_2O_3 lattice. Conversely, the single-layer nature of model (I) with its two Ce protrusions per unit cell is neither consistent with the type-C structures nor with the experimentally observed (2×2) reconstruction. This suggests that, despite the highly reducing conditions of the experiment, a complete transition from calcium-fluorite to bixbyite ceria has not yet occurred in the nanoparticles, justifying their description with surface-reduced CeO_2 models.

3. CONCLUSIONS

Well-shaped ceria crystallites exposing wide (100) facets have been prepared by annealing a Ru-supported CeO_2(111) film to temperatures above 800 K. Two surface reconstructions were identified that both compensate for the electrostatic dipole of the bulk-cut (100) plane. While the main (2×2) phase is composed of pyramidal CeO_4 units, similar to the Wolf reconstruction, an O termination has been determined for a c(2×2) minority phase. Both structures are further stabilized by oxygen removal from the stoichiometric surfaces. A gradual reduction of the ceria lattice is also relevant for explaining the shape evolution of the nanoparticles upon thermal treatment.

The ceria crystallites analyzed here open an interesting route to explore adsorption phenomena and chemical reactivity of open and polar oxide surfaces in the future.

4. EXPERIMENT and THEORY

All experiments were carried out in a liquid-helium cooled STM equipped with standard tools for sample preparation and analysis. Ceria crystallites with desired (100) termination were produced in a two-step procedure. First, a (111)-oriented CeO_2 film of five trilayer thickness was grown by depositing elemental cerium in 1×10^{-6} mbar O_2 onto a sputtered and annealed Ru(0001) surface at 300 K.[12] The deposition rate was set to 0.2 trilayer /min. In a subsequent annealing step to 800 - 1100 K in 1×10^{-6} mbar of oxygen, the compact film was converted into an assembly of oxide crystallites exposing wide (100) facets.

Structure and stability of these facets were analyzed with DFT+U calculations as implemented in VASP.[31, 32] The U-J parameter was set to 4.5 eV.[33] The interaction between valence electrons and ionic cores was treated with the projector augmented wave method.[34, 35] The Kohn-Sham orbitals were developed on a plane-wave basis set with 400 eV energy cut-off. Ceria surfaces with (2×2) unit cells have been modeled on eight-layer thick, asymmetric (100) slabs. One side of the slab was covered with ½ oxygen monolayer, while the other exposed the surface structure of interest. To avoid spurious interactions between periodic images, the slabs were separated by 10 Å of vacuum and a dipole correction scheme was applied. A (3×3×1) Monkhorst Pack grid was used for k-point sampling of the Brillouin zone. The positions of all atoms in the five topmost layers of the slab were relaxed until residual forces dropped below 0.01 eV/Å.

ACKNOWLEDGMENT: The work was supported by the DFG excellence cluster ‘UNICAT’ and the COST Action CM1104 ‘Reducible oxides’.

REFERENCES

[1] Catalysis by Ceria and Related Materials. Catalytic Science Series. vol. 2; Trovarelli, A. Eds.; Imperial College Press: London, 2002.

[2] N. V. Skorodumova, S. I. Simak, B. I. Lundqvist, I. A. Abrikosov, B. Johansson, *Phys. Rev. Lett.* **2002**, *89*, 166601.

[3] Dean C. Sayle, S. Andrada Maicaneanu, Graeme W. Watson, *J. Am. Chem. Soc.* **2002**, *124*, 11429.

[4] J. C. Conesa, *Surf. Sci.* **1995**, *339*, 337.

[5] N. V. Skorodumova, M. Baudin, K. Hermansson, *Phys. Rev. B* **2004**, *69*, 075401.

[6] M. Fronzi, A. Soon, B. Delley, E. Traversa, C. Stampfl, *J. Chem. Phys.* **2009**, *131*, 104701.

[7] D. R. Mullins, P. M. Albrecht, T.-L. Chen, F. C. Calaza, M. D. Biegalski, H. M. Christen, S. H. Overbury, *J. Phys. Chem. C* **2012**, *116*, 19419.

[8] H. –T. Chen, Y. M. Choi, M. Liu, and M. C. Lin, *Chem. Phys. Chem.* **2007**, *8*, 849.

[9] T. X. T. Sayle, S. C. Parker, D. C. Sayle, *Phys. Chem. Chem. Phys.* **2005**, *7*, 2936.

[10] V. Matolin, J. Libra, I. Matolinova, V. Nehasil, L. Sedlacek, F. Sutara, *Appl. Surf. Sci.* **2007**, *254*, 153.

[11] P. Luches, F. Pagliuca, S. Valeri, *J. Phys. Chem. C* **2011**, *115*, 10718.

[12] J. F. Jerratsch, X. Shao, N. Nilius, H. J. Freund, C. Popa, M. V. Ganduglia-Pirovano, A. M. Burow, J. Sauer, *Phys. Rev. Lett.* **2011**, *106*, 246801.

[13] F. Zhang, S.-W. Chan, J. E. Spanier, E. Apak, Q. Jin, R. D. Robinson, I. P. Herman, *Appl. Phys. Lett.* **2002**, *80*, 127.

[14] A. S. Barnard, A. I. Kirkland, *Chem. Mater.* **2008**, *20*, 5460.

[15] P. Zhao, A. Ito, R. Tu, T. Goto, *Surf. Coat. Tech.* **2011**, *205*, 4079.

[16] J. Goniakowski, F. Finocchi, C. Noguera, *Rep. Prog. Phys.* **2008**, *71*, 016501.

[17] H. Nörenberg, J. H. Harding, STM. *Surf. Sci.* **2001**, *477*, 17.

[18] U. M. Bhatta, I. M. Ross, T. X. T. Sayle, D. C. Sayle, S. C. Parker, D. Reid, S. Seal, A. Kumar, G. Möbus, *ACS Nano.* **2012**. *6*, 421.

[19] Y. Lin, Z. Wu, J. Wen, K. R. Poeppelmeier, L. D. Marks, *Nano Lett.* **2014**, *14*, 191.

[20] R. F. B. De Souza, A. E. A. Flausino, D. C. Rascio, R. T. S. Oliveira, E. Neto, M. L. Calegaro, M. C. Santos. *Appl. Catal. B* **2009**, *91*, 516.

[21] B. Kaemena, S. D. Senanayake, A. Meyer, J. T. Sadowski, J. Falta, J. I. Flege, *J. Phys. Chem. C* **2013**, *117*, 221.

[22] T. Hasegawa, S. M. F. Shahed,.Y. Sainoo, A. Beniya, N. Isomura, Y. Watanabe, T. Komeda, *J. Chem. Phys.* **2014**, *140*, 044711.

[23] M. Baudin, M. Wojcik, K. Hermansson, *Surf. Sci.* **2000**, *468*, 51.

[24] Z. Yang, T. K. Woo, M. Baudin, K. Hermansson, *J. Chem. Phys.* **2004**, *120*, 7741.

[25] M. Nolan, S. Grigoleit, D. C. Sayle, S. C. Parker, G. W. Watson, *Surf. Sci.* **2005**, *576*, 217.

[26] G. S. Herman, *Phys. Rev. B* **1999**, *59*, 14899.

[27] O. Stetsovych, J. Beran, F. Dvorák, K. Masek, J. Myslivecek, V. Matolín, *Appl. Surf. Sci.* **2013**, *285*, 766.

[28] D. Wolf, *Phys. Rev. Lett.* **1992**, *68*, 3315.

[29] A. Barbier, C. Mocuta, H. Kuhlenbeck, K. F. Peters, B. Richter, G. Renaud, *Phys. Rev. Lett.* **2000**, *84*, 2897.

[30] G. Wulff, *Z. Krist.* **1901**. *34*, 449.

[31] M. V. Ganduglia-Pirovano, J. L. F. Da Silva, J. Sauer, *Phys. Rev. Lett.* **2009**, *102*, 026101.

[32] G. Kresse, J. Furthmuller, *Phys. Rev. B* **1996**, *54*, 11169.

[33] J. L. F. Da Silva, M. V. Ganduglia-Pirovano, J. Sauer, V. Bayer, G. Kresse, *Phys. Rev. B* **2007**, *75*, 045121.

[34] P. E. Blochl, *Phys. Rev. B* **1994**, *50*, 17953.

[35] G. Kresse, J. Joubert, *Phys. Rev. B* **1999**, *59*, 1758.